UNIVERSITY OF AMSTERDAM

UvA-DARE (Digital Academic Repository)

X-Ray Polarization Detection of the Pulsar Wind Nebula in G21.5-0.9 with IXPE

Di Lalla, Niccolò; Ng, C.Y.; Vink, Jacco; IXPE

DOI
10.3847/1538-4357/adf6b5

Publication date
2025

Document Version
Final published version

Published in
Astrophysical Journal

License
CC BY

Link to publication

Citation for published version (APA):
Di Lalla, N., Ng, C. Y., Vink, J., & IXPE (2025). X-Ray Polarization Detection of the Pulsar Wind Nebula in G21.5-0.9 with IXPE. *Astrophysical Journal*, *991*(1), Article 67. https://doi.org/10.3847/1538-4357/adf6b5

General rights
It is not permitted to download or to forward/distribute the text or part of it without the consent of the author(s) and/or copyright holder(s), other than for strictly personal, individual use, unless the work is under an open content license (like Creative Commons).

Disclaimer/Complaints regulations
If you believe that digital publication of certain material infringes any of your rights or (privacy) interests, please let the Library know, stating your reasons. In case of a legitimate complaint, the Library will make the material inaccessible and/or remove it from the website. Please Ask the Library: https://uba.uva.nl/en/contact, or a letter to: Library of the University of Amsterdam, Secretariat, P.O. Box 19185, 1000 GD Amsterdam, The Netherlands. You will be contacted as soon as possible.

UvA-DARE is a service provided by the library of the University of Amsterdam (https://dare.uva.nl)

Download date:13 Oct 2026

The Astrophysical Journal, 991:67 (12pp), 2025 September 20 https://doi.org/10.3847/1538-4357/adf6b5
© 2025. The Author(s). Published by the American Astronomical Society.
OPEN ACCESS

X-Ray Polarization Detection of the Pulsar Wind Nebula in G21.5–0.9 with IXPE

Niccolò Di Lalla[1,2], Nicola Omodei[1,2], Niccolò Bucciantini[3,4,5], Jack T. Dinsmore[2], Nicolò Cibrario[6,7], Stefano Silvestri[8], Josephine Wong[2], Patrick Slane[9], Tsunefumi Mizuno[10], Michela Negro[11], Roger W. Romani[2], Riccardo Ferrazzoli[12], C.-Y. Ng[13], Miltiadis Michailidis[1,2], Yi-Jung Yang[14,15], Fei Xie[12,16], Martin C. Weisskopf[17], Philip Kaaret[17], Iván Agudo[18], Lucio A. Antonelli[19,20], Matteo Bachetti[21], Luca Baldini[8,22], Wayne H. Baumgartner[23], Ronaldo Bellazzini[8], Stefano Bianchi[24], Stephen D. Bongiorno[17], Raffaella Bonino[6,7], Alessandro Brez[8], Fiamma Capitanio[12], Simone Castellano[8], Elisabetta Cavazzuti[25], Chien-Ting Chen[26], Stefano Ciprini[20,27], Enrico Costa[12], Alessandra De Rosa[12], Ettore Del Monte[12], Laura Di Gesu[25], Alessandro Di Marco[12], Immacolata Donnarumma[25], Victor Doroshenko[28], Michal Dovčiak[29], Steven R. Ehlert[17], Teruaki Enoto[30], Yuri Evangelista[12], Sergio Fabiani[12], Javier A. Garcia[31], Shuichi Gunji[32], Jeremy Heyl[33], Wataru Iwakiri[34], Svetlana G. Jorstad[35,36], Vladimir Karas[29], Fabian Kislat[37], Takao Kitaguchi[30], Jeffery J. Kolodziejczak[17], Henric Krawczynski[38], Fabio La Monaca[12,39], Luca Latronico[6], Ioannis Liodakis[40], Simone Maldera[6], Alberto Manfreda[41], Frédéric Marin[42], Andrea Marinucci[25], Alan P. Marscher[35], Herman L. Marshall[43], Francesco Massaro[6,7], Giorgio Matt[24], Ikuyuki Mitsuishi[44], Fabio Muleri[12], Stephen L. O'Dell[17], Chiara Oppedisano[6], Alessandro Papitto[19], George G. Pavlov[45], Abel Lawrence Peirson[2], Matteo Perri[19,20], Melissa Pesce-Rollins[8], Pierre-Olivier Petrucci[46], Maura Pilia[21], Andrea Possenti[21], Juri Poutanen[47], Simonetta Puccetti[20], Brian D. Ramsey[17], John Rankin[48], Ajay Ratheesh[12], Oliver J. Roberts[26], Carmelo Sgró[8], Paolo Soffitta[12], Gloria Spandre[8], Douglas A. Swartz[26], Toru Tamagawa[30], Fabrizio Tavecchio[48], Roberto Taverna[49], Yuzuru Tawara[44], Allyn F. Tennant[17], Nicholas E. Thomas[17], Francesco Tombesi[27,39], Alessio Trois[21], Sergey Tsygankov[50], Roberto Turolla[49,51], Jacco Vink[52], Kinwah Wu[51], and Silvia Zane[51]

[1] W. W. Hansen Experimental Physics Laboratory (HEPL), Stanford University, Stanford, CA 94305, USA; niccolo.dilalla@stanford.edu
[2] Department of Physics and Kavli Institute for Particle Astrophysics and Cosmology, Stanford University, Stanford, CA 94305, USA
[3] INAF Osservatorio Astrofisico di Arcetri, Largo Enrico Fermi 5, 50125 Firenze, Italy
[4] Dipartimento di Fisica e Astronomia, Università degli Studi di Firenze, Via Sansone 1, 50019 Sesto Fiorentino (FI), Italy
[5] Istituto Nazionale di Fisica Nucleare, Sezione di Firenze, Via Sansone 1, 50019 Sesto Fiorentino (FI), Italy
[6] Istituto Nazionale di Fisica Nucleare, Sezione di Torino, Via Pietro Giuria 1, 10125 Torino, Italy
[7] Dipartimento di Fisica, Università degli Studi di Torino, Via Pietro Giuria 1, 10125 Torino, Italy
[8] Istituto Nazionale di Fisica Nucleare, Sezione di Pisa, Largo B. Pontecorvo 3, 56127 Pisa, Italy
[9] Center for Astrophysics—Harvard & Smithsonian, 60 Garden Street, Cambridge, MA 02138, USA
[10] Hiroshima Astrophysical Science Center, Hiroshima University, 1-3-1 Kagamiyama, Higashi-Hiroshima, Hiroshima 739-8526, Japan
[11] Department of Physics and Astronomy, Louisiana State University, Baton Rouge, LA 70803, USA
[12] INAF Istituto di Astrofisica e Planetologia Spaziali, Via del Fosso del Cavaliere 100, 00133 Roma, Italy
[13] Department of Physics, The University of Hong Kong, Pokfulam, Hong Kong
[14] Graduate Institute of Astronomy, National Central University, 300 Zhongda Road, Zhongli, Taoyuan 32001, Taiwan
[15] Laboratory for Space Research, The University of Hong Kong, Cyberport 4, Hong Kong
[16] Guangxi Key Laboratory for Relativistic Astrophysics, School of Physical Science and Technology, Guangxi University, Nanning 530004, People's Republic of China
[17] NASA Marshall Space Flight Center, Huntsville, AL 35812, USA
[18] Instituto de Astrofísica de Andalucía—CSIC, Glorieta de la Astronomía s/n, 18008 Granada, Spain
[19] INAF Osservatorio Astronomico di Roma, Via Frascati 33, 00078 Monte Porzio Catone (RM), Italy
[20] Space Science Data Center, Agenzia Spaziale Italiana, Via del Politecnico snc, 00133 Roma, Italy
[21] INAF Osservatorio Astronomico di Cagliari, Via della Scienza 5, 09047 Selargius (CA), Italy
[22] Dipartimento di Fisica, Università di Pisa, Largo B. Pontecorvo 3, 56127 Pisa, Italy
[23] Naval Research Laboratory, 4555 Overlook Ave. SW, WA, DC 20375, USA
[24] Dipartimento di Matematica e Fisica, Università degli Studi Roma Tre, Via della Vasca Navale 84, 00146 Roma, Italy
[25] ASI – Agenzia Spaziale Italiana, Via del Politecnico snc, 00133 Roma, Italy
[26] Science and Technology Institute, Universities Space Research Association, Huntsville, AL 35805, USA
[27] Istituto Nazionale di Fisica Nucleare, Sezione di Roma "Tor Vergata," Via della Ricerca Scientifica 1, 00133 Roma, Italy
[28] Institut für Astronomie und Astrophysik, Universität Tübingen, Sand 1, 72076 Tübingen, Germany
[29] Astronomical Institute of the Czech Academy of Sciences, Boční II 1401/1, 14100 Praha 4, Czech Republic
[30] RIKEN Cluster for Pioneering Research, 2-1 Hirosawa, Wako, Saitama 351-0198, Japan
[31] NASA Goddard Space Flight Center, Greenbelt, MD 20771, USA
[32] Yamagata University, 1-4-12 Kojirakawa-machi, Yamagata-shi 990-8560, Japan
[33] University of British Columbia, Vancouver, BC V6T 1Z4, Canada
[34] International Center for Hadron Astrophysics, Chiba University, Chiba 263-8522, Japan
[35] Institute for Astrophysical Research, Boston University, 725 Commonwealth Avenue, Boston, MA 02215, USA
[36] Department of Astrophysics, St. Petersburg State University, Universitetsky pr. 28, Petrodvoretz, 198504 St. Petersburg, Russia
[37] Department of Physics and Astronomy and Space Science Center, University of New Hampshire, Durham, NH 03824, USA
[38] Physics Department and McDonnell Center for the Space Sciences, Washington University in St. Louis, St. Louis, MO 63130, USA
[39] Dipartimento di Fisica, Università degli Studi di Roma "Tor Vergata," Via della Ricerca Scientifica 1, 00133 Roma, Italy
[40] Institute of Astrohysics, FORTH, N. Plastira 100, GR-70013 Vassilika Vouton, Greece
[41] Istituto Nazionale di Fisica Nucleare, Sezione di Napoli, Strada Comunale Cinthia, 80126 Napoli, Italy
[42] Université de Strasbourg, CNRS, Observatoire Astronomique de Strasbourg, UMR 7550, 67000 Strasbourg, France
[43] MIT Kavli Institute for Astrophysics and Space Research, Massachusetts Institute of Technology, 77 Massachusetts Avenue, Cambridge, MA 02139, USA
[44] Graduate School of Science, Division of Particle and Astrophysical Science, Nagoya University, Furo-cho, Chikusa-ku, Nagoya, Aichi 464-8602, Japan
[45] Department of Astronomy and Astrophysics, Pennsylvania State University, University Park, PA 16802, USA

[46] Université Grenoble Alpes, CNRS, IPAG, 38000 Grenoble, France
[47] Department of Physics and Astronomy, University of Turku, FI-20014, Finland
[48] INAF Osservatorio Astronomico di Brera, Via E. Bianchi 46, 23807 Merate (LC), Italy
[49] Dipartimento di Fisica e Astronomia, Università degli Studi di Padova, Via Marzolo 8, 35131 Padova, Italy
[50] Department of Physics and Astronomy, University of Turku, FI 20014, Finland
[51] Mullard Space Science Laboratory, University College London, Holmbury St Mary, Dorking, Surrey, RH5 6NT, UK
[52] Anton Pannekoek Institute for Astronomy & GRAPPA, University of Amsterdam, Science Park 904, 1098 XH Amsterdam, The Netherlands
Received 2025 April 28; revised 2025 July 29; accepted 2025 July 30; published 2025 September 17

Abstract

We present the X-ray polarization observation of G21.5−0.9, a young Galactic supernova remnant (SNR), conducted with the Imaging X-ray Polarimetry Explorer (IXPE) in 2023 October, with a total livetime of approximately 837 ks. Using different analysis methods, such as a space-integrated study of the entire region of the pulsar wind nebula (PWN) and a space-resolved polarization map, we detect significant polarization from the PWN at the center of the SNR, with an average polarization degree of ∼10% oriented at ∼33° (north through east). No significant energy-dependent variation in polarization is observed across the IXPE band (2–8 keV). The polarization map, corrected for the effect of polarization leakage, reveals a consistent pattern in both degree and angle, with little change across the nebula. Our findings indicate the presence of a highly polarized central torus, suggesting low levels of turbulence at particle acceleration sites. Unlike Vela, but similar to the Crab Nebula, we observe substantial differences between radio and X-ray polarization maps. This suggests a clear separation in energy of the emitting particle populations and hints at an important, yet poorly understood, role of instabilities in the turbulence dynamics of PWNe.

Unified Astronomy Thesaurus concepts: Pulsar wind nebulae (2215); Pulsars (1306); Polarimetry (1278); X-ray astronomy (1810)

1. Introduction

Pulsars are strongly magnetized and rapidly rotating neutron stars, born from the explosive deaths of massive stars, first discovered by Jocelyn Bell Burnell in 1967 using the Interplanetary Scintillation Array radio telescope in Cambridge, UK (A. Hewish et al. 1968). As pulsars spin around their axes, they unleash powerful beams of radiation and a persistent powerful stream of relativistic particles into space. These emitted particles, which together with the Poynting flux form the so-called pulsar wind, are accelerated to nearly the speed of light by the intense magnetic and electric fields present in the magnetosphere. As they propagate along the magnetic field lines, they interact with the surrounding interstellar medium or supernova ejecta. This interaction creates shock fronts, and gives rise to an extended and complex synchrotron-emitting nebula, from radio to X-ray and MeV energies, called a pulsar wind nebula (PWN; B. M. Gaensler & P. O. Slane 2006). PWNe constitute an incredibly fascinating laboratory for exploring fundamental physics in conditions not replicable on Earth, providing valuable insights into relativistic shocks and particle acceleration processes governing the dynamics of relativistic outflows and their influence on the surrounding interstellar environment.

G21.5−0.9 is a young, composite *plerionic* supernova remnant (SNR) characterized in X-rays by the presence of a central, bright, 40″-radius PWN surrounded by a much dimmer and softer SNR shell (P. Slane et al. 2000; S. Safi-Harb et al. 2001). Deep observations obtained with Chandra X-ray Observatory (CXO) and XMM-Newton have revealed that the SNR blast wave extends up to 150″ and displays a limb-brightening feature at the eastern boundary and knots of enhanced soft X-ray emission above the PWN in the northern direction (F. Bocchino et al. 2005; H. Matheson & S. Safi-Harb 2005; H. Matheson & S. Safi-Harb 2010; B. T. Guest et al. 2019). Observations of G21.5−0.9 across various electromagnetic wavelengths, from radio to γ-rays, have unveiled a wealth of information about this source. Using the Very Large Array (VLA) to measure its expansion speed, M. F. Bietenholz & N. Bartel (2008) estimated its age to be ∼870 yr, making G21.5−0.9 one of the youngest PWNe known in our Galaxy. Its distance to Earth was measured by several authors using different techniques, and was found to be around 5 kpc (S. Safi-Harb et al. 2001; F. Camilo et al. 2006; M. F. Bietenholz & N. Bartel 2008; W. W. Tian & D. A. Leahy 2008). The first maps at radio wavelengths go back to the 1970s and '80s (R. H. Becker & M. R. Kundu 1976; A. S. Wilson & K. W. Weiler 1976; E. Furst et al. 1988), but even more recent deep searches have failed to detect a radio counterpart of the X-ray SNR shell, with the exception of the northern knot (M. F. Bietenholz et al. 2011).

At the heart of G21.5−0.9 lies the pulsar PSR J1833−1034, first independently discovered in radio by Y. Gupta et al. (2005) and F. Camilo et al. (2006), who found a compact pulsating source at the center of the PWN (R.A. = $18^{h}33^{m}33\overset{s}{.}57$, decl. = −10°34′07″.5 (J2000.0)) with period $P = 61.86$ ms, $\dot{P} = 2 \times 10^{-13}$, a surface magnetic field of $B = 3.6 \times 10^{12}$ G, a characteristic age of 4.8 kyr, and a spin-down luminosity of $\dot{E} = 3.3 \times 10^{37}$ erg s^{-1}. The pulsar remains currently undetected at X-ray energies, while γ-ray pulsation has been detected with the Fermi Large Area Telescope (A. A. Abdo et al. 2013; D. A. Smith et al. 2023). Past X-ray observations have only led to upper limits on the pulsating fraction, while still detecting a central compact source surrounded by an elliptical emission region (P. Slane et al. 2000; S. Safi-Harb et al. 2001; F. Camilo et al. 2006). The projected spin-axis direction of PSR J1833−1034, inferred by fitting the pulsar wind torus using CXO data, was determined to be at a position angle of 45° ± 1° north through east (C. Y. Ng & R. W. Romani 2008).

Original content from this work may be used under the terms of the Creative Commons Attribution 4.0 licence. Any further distribution of this work must maintain attribution to the author(s) and the title of the work, journal citation and DOI.

Polarization observations can play a crucial role in unraveling the complex structure of PWNe like G21.5−0.9, by offering unique insights into the physical processes at play within these astrophysical sources. Polarimetry, in fact, provides essential information about magnetic fields, particle acceleration mechanisms, and the overall dynamics of these systems, contributing to a more comprehensive understanding of the intricate interplay between pulsars and their cosmic surroundings.

The initial radio polarization maps of G21.5−0.9 were obtained by R. H. Becker & A. E. Szymkowiak (1981) with the VLA and by E. Furst et al. (1988) using the NRO Millimeter-wave Array, and revealed a highly ordered, linearly polarized emission distributed in a ring structure, indicating a radial magnetic field configuration. The level of polarization was found to have a minimum toward the center, where little polarization was detected, and to increase with radius up to 20%–30% near the boundary of the PWN. Infrared polarimetric observations performed with the Very Large Telescope on the compact core of the PWN (angular size $\lesssim 5''$) revealed a highly polarized emission, with an average value of the linear polarization degree of ∼47%, and a swing of the polarization angle across the inner nebula consistent with a toroidal magnetic field (A. Zajczyk et al. 2012). On the other hand, a recent polarimetric study by P. C. W. Lai et al. (2022), using archival high-resolution radio observations taken with VLA, confirmed the global radial magnetic field structure of the PWN and ruled out the existence of any strong large-scale toroidal field components extending beyond the inner nebula.

Unlike Crab, Vela, or MSH 15−52 (F. Xie et al. 2022; R. W. Romani et al. 2023; N. Bucciantini et al. 2023b), which in X-rays all display a morphology dominated by a jet-torus structure, G21.5−0.9 has a much more amorphous appearance, the torus is barely evident, and there is no sign of a jet. Moreover, among the PWNe that can be resolved by the Imaging X-ray Polarimetry Explorer (IXPE), G21.5−0.9 is the only one that shows a tangential polarization pattern in radio. In this regard, this source represents a system quite different from the ones studied previously, and X-ray polarimetry could provide insight to better understand such a difference.

This paper is structured as follows. In Section 2, we present the IXPE observation of G21.5−0.9, together with the initial processing done on the data. Section 3 is dedicated to a description of the different types of polarization analyses performed and to the presentation of the main results. The implications and possible physical interpretation of these results are discussed in Section 4. Finally, Appendices A and B contain, respectively, additional plots of the polarization analysis and a review of the methods used to evaluate or subtract the effect of polarization leakage.

2. Observations

IXPE, successfully launched on 2021 December 9, is the first space observatory entirely dedicated to imaging polarimetry in X-rays (M. C. Weisskopf et al. 2022). The result of an international collaboration between NASA and the Italian Space Agency (ASI), IXPE is provided with three identical but independent telescopes, each equipped with a Gas Pixel Detector (GPD) at its focal plane (R. Bellazzini et al. 2006; L. Baldini et al. 2021), housed inside a detector unit (DU).

IXPE observed G21.5−0.9 in three separate segments close in time and combined in a single observation with a total livetime of ∼837 ks: the first segment lasted from 2023 October 5 at 00:05:39.233 UTC to 2023 October 9 at 02:16:33.292 UTC, the second one from 2023 October 10 at 22:45:54.503 UTC to 2023 October 17 at 16:42:55.034 UTC, and the last one from 2023 October 19 at 21:35:44.584 UTC to 2023 October 27 at 15:39:00.534 UTC. IXPE Level-2 data, publicly available for download on the HEASARC archive[53] (ObsID 02001199), were reprocessed and analyzed according to the standard technique using the version `20240125` of the IXPE instrument response functions (IRFs) released on the CALDB[54] on 2024 February 28 (validity date `20230702`). Given the temporal proximity and relatively short total duration of the IXPE observations, spanning less than a month, and the known variability timescale of the nebula, which is on the order of several months to years (B. T. Guest et al. 2019), G21.5−0.9 can be considered effectively steady for the purpose of this analysis.

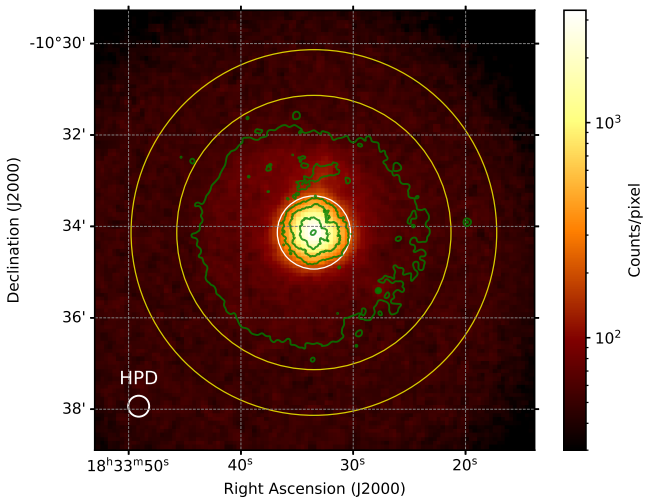

Figure 1. IXPE smoothed count map of G21.5−0.9 in logarithmic scale, obtained by combining the data from the three DUs (2–8 keV). In green are the contours from the deep CXO merged observations (0.5–8 keV), described in the text and visible as a background image of Figure 3. The white circle and yellow annulus indicate, respectively, the source and background extraction regions used for the polarization analysis described in Section 3.1. At the bottom-left corner is the IXPE half-power diameter HPD ∼ 25″ for DU1 for reference.

Before analyzing the data, we performed an initial background rejection following the procedure described in A. Di Marco et al. (2023) to reduce the instrumental background due to cosmic-ray particles interacting in the GPD by approximately 40%. We also excluded approximately 4 ks of total livetime (∼0.5%) affected by sudden spikes in the counting rate over short time intervals, likely associated with solar activity and the boundary of the South Atlantic Anomaly. In addition, we corrected the absolute sky coordinates by adjusting the World Coordinate System keywords in the FITS header to align the reference frame with that of CXO (`TCRPX7 = 304`, `TCRPX8 = 301.5`). These are the data files used from now on in this paper. Figure 1 shows the count map resulting from the combination of the three IXPE telescopes over the full energy range (2–8 keV). The white circular region (radius 0.′8 centered on the pulsar location) is used to select the inner PWN, while the yellow annulus (inner/

[53] https://heasarc.gsfc.nasa.gov/docs/ixpe/archive/
[54] https://heasarc.gsfc.nasa.gov/docs/ixpe/caldb/

Table 1
List of the CXO ObsIDs Used

ObsID	Exposure (ks)	ObsID	Exposure (ks)
159	14.85	3700	9.54
1230	14.56	5159	9.83
1433	14.97	5166	10.02
1554	9.06	6071	9.64
1717	7.54	6741	9.83
1770	7.22	8372	10.01
1838	7.85	10646	9.54
2873	9.83	14263	9.57
3693	9.78	16420	9.57

Note. List of ObsIDs and their exposure for the CXO observations used to produce the count map used as background in all polarization maps shown in the paper (e.g., Figure 3) and whose contours are shown in Figure 1. The total exposure is around 183 ks. The CXO data sets are contained in the Chandra Data Collection (DOI: 10.25574/cdc.425).

outer radii of 3′ and 4′ from the pulsar) defines the background extraction region used for the space-integrated analysis described in Section 3.1.

G21.5−0.9 is observed with CXO routinely as a calibration source. Overlaid in green in Figure 1 are the contours of a deep image created by merging 18 individual observations listed in Table 1 (total exposure ∼183 ks) and contained in the Chandra Data Collection (doi:10.25574/cdc.425), all of which had the remnant placed in the ACIS-S detector, at the default aimpoint of the S3 CCD chip. The events were combined with the `merge_obs` script in the `ciao`[55] analysis software. A count map was then created using events in the 0.5–8.0 keV energy band, and adaptively smoothed with the `dmimgadapt` tool using a cone filter with minimum/maximum smoothing radii of 0.″5 and 150″ spanning 300 logarithmically spaced scales, with a minimum of 75 counts within the smoothing kernel. The resulting map is used as background image in all polarization maps shown throughout the paper.

3. Polarization Analysis

In this section, we describe the different analysis methods used to measure the polarization of G21.5−0.9. We performed two main types of analysis: an integrated study of the entire region of the PWN (Section 3.1), and a space-resolved measurement aimed at mapping the polarization pattern across the nebula (Section 3.2).

3.1. Space-integrated Analysis

As is typically done for other IXPE observations (F. Xie et al. 2022; N. Bucciantini et al. 2023b; M. Negro et al. 2023), using the spatial regions described at the end of Section 2 and shown in Figure 1, we studied the polarization of the entire PWN in two different ways: a model-independent polarimetric analysis using IXPEOBSSIM (L. Baldini et al. 2022), and a spectropolarimetric fit with the Multi-Mission Maximum Likelihood (`3ML`) framework (G. Vianello et al. 2015). For the former, we utilized the `xpselect` and `xpbin` applications of IXPEOBSSIM (v31.0.1) to first select photons belonging to the source and background regions, and then binned the filtered data files using the `PCUBE` algorithm (unweighted analysis). This binning routine combines the event-by-event Stokes parameters, subtracts the background contribution, and computes the degree (PD) and angle (PA) of polarization of the source, along with the associated errors, according to the procedure of F. Kislat et al. (2015). PA represents the electric vector position angle and is conventionally defined counterclockwise relative to the local north (toward northeast). Combining the data from the three IXPE DUs over the 2–8 keV energy range, we measured with this method a PD of 10.2% ± 1.5% for the PWN, with a PA of 33° ± 4°. The corresponding minimum detectable polarization (MDP) at 99% confidence is $\mathrm{MDP}_{99\%} = 4.3\%$ (M. C. Weisskopf et al. 2010), well below the detected level polarization. The measured PA is broadly consistent with the spin-axis direction of PSR J1833−1034, although in tension at a 3σ level. To investigate possible energy dependence, we repeated the analysis in two energy bands, 2–4 keV and 4–8 keV, and found no significant variation in polarization, with results consistent within uncertainties. As an internal consistency check, we also repeated the analysis independently for each DU, and found agreement within 1σ for both PD and PA. The results for the combined DUs are summarized on the left side of Table 2 and visualized in Figure 2.

For the spectropolarimetric analysis, instead, we started from the same filtered data, produced earlier for the source and background regions, and used the `xpbin` application (algorithms `PHA1`, `PHA1Q`, and `PHA1U`; unweighted analysis) to compute the Stokes I, Q, and U spectra for the three DUs. These files can then be jointly fit in `3ML` or XSPEC[56] to simultaneously recover the spectral and polarimetric parameters of the user-defined models. For G21.5−0.9, we modeled the observed spectrum with an absorbed power law, with absorption given by the `TbAbs`[57] model with `wilm` abundances (J. Wilms et al. 2000). According to what was found by B. T. Guest et al. (2019), the column density parameter was fixed to the value $N_{\mathrm{H}} = 3.237 \times 10^{22}$ cm^{-2}. Regarding the polarimetric model, based on the result of the previous `PCUBE` analysis, we chose to employ a model with a constant degree and angle of polarization. To account for potential cross-calibration uncertainties among the different IXPE telescopes, we also added and left free to vary a multiplicative normalization constant for DU2 and DU3 relative to DU1. The best-fit results obtained using `3ML` are provided on the right side of Table 2. The power-law index we measured is $\Gamma = 1.92 \pm 0.02$, slightly higher than the value reported by B. T. Guest et al. (2019), most likely due to contamination from the much softer external halo and differences in the source extraction region. In support of this interpretation, our spectral result is in good agreement with the analysis by M. Tsujimoto et al. (2011), which used a much larger extraction radius (165″) encompassing the entire remnant. Note that the quoted uncertainty represents the statistical error only and does not account for possible systematic effects from instrumental calibration (see Appendix A for further discussion). The unabsorbed flux (2–8 keV) is $F_{2-8\mathrm{keV}} = (3.91 \pm 0.03) \times 10^{-11}$ erg s^{-1} cm^{-2}. The polarimetric results agree well with those from the `PCUBE` analysis, with a best-fit PD = 9.7% ± 1.2% and PA = 32° ± 4°. Figure 2 gives a

[55] https://cxc.cfa.harvard.edu/ciao/

[56] https://heasarc.gsfc.nasa.gov/xanadu/xspec/

[57] https://astromodels.readthedocs.io/en/latest/notebooks/TbAbs.html

Table 2
Summary of the Space-integrated Analysis of the PWN

Parameter	Energy Range	Value	Parameter	Value
⋯	2–8 keV	10.2% ± 1.5%	$N_{\rm H}$ (fixed)	3.237×10^{22} cm^{-2}
PD	2–4 keV	9.7% ± 1.5%	Γ	1.92 ± 0.02
⋯	4–8 keV	11.3% ± 2.5%	PD	9.7% ± 1.2%
⋯	2–8 keV	33° ± 4°	PA	32° ± 4°
PA	2–4 keV	36° ± 4°	Q/I	0.041 ± 0.012
⋯	4–8 keV	28° ± 7°	U/I	0.087 ± 0.012

Note. Summary table of the PCUBE analysis (left) and spectropolarimetric fit (right) of the space-integrated PWN. Errors are statistical only at a 1σ level. The spectropolarimetric fit is performed using 3ML in the 2–8 keV energy range assuming Gaussian statistics and results in a reduced chi-square value of χ^2/d.o.f. = 1462.6/1353 (p-value = 0.02).

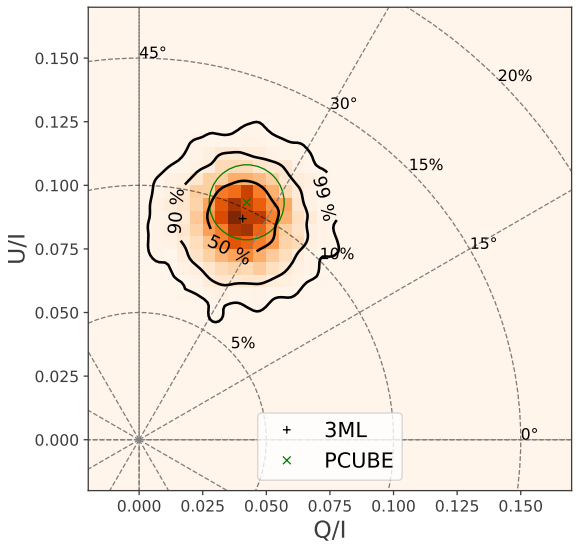

Figure 2. Q/I vs. U/I plot showing the results of the space-integrated polarization analysis of the PWN in the 2–8 keV energy range. In orange shades, the 2D distribution resulting from the spectropolarimetric analysis with the 50%, 90%, and 99% confidence level contours in black and the + marker indicating the best-fit parameters. The green × and circle show, respectively, the result of the PCUBE analysis and the associated 1σ error.

summary of the main results of the space-integrated polarimetric analysis of the PWN.

3.2. Space-resolved Analysis

To map the polarization of G21.5−0.9 in the PWN region, we again used the xpbin tool of IXPEOBSSIM, this time with the PMAP algorithm. This routine processes the provided data files by binning the Stokes parameters I, Q, and U in sky coordinates, thus allowing us to measure the polarization pattern across the field of view. In particular, we binned the data using a grid of 90 × 90 squared pixels, each with a side of $0.'1944$, considering photons with energies in the full IXPE energy band (2–8 keV). Then, we used the implemented methods to perform a 2D convolution of the original Stokes maps with a unit-filled 3 × 3 kernel matrix, assigning to each pixel the sum of the contents of itself and its eight neighbors. In this way, adjacent pixels become highly correlated and the effective size of the pixel triples and becomes comparable to the IXPE angular resolution (half-power diameter $\sim 25''$–$30''$), while still maintaining the original binning grid.

Since the start of the IXPE mission, it has been well known that imperfections in reconstructing photon absorption points within the GPD, arising from the event reconstruction algorithm (L. Baldini et al. 2021) or from the finite spatial resolution of the GPD, can produce a radially polarized halo around the source, commonly referred to as polarization leakage (for a detailed overview of the effect, see N. Bucciantini et al. 2023a). Being an intrinsic effect of the detector or its reconstruction algorithm, this phenomenon is present in all IXPE observations, but in practice it is only really relevant for the analysis of a handful of bright extended sources, which exhibit a very sharp intensity gradient. Since the polarization pattern induced by the leakage is radial, its contribution effectively averages out when selecting a circular region that includes the entire source, as done in Section 3.1. For the space-resolved polarization analysis, instead, polarization leakage can strongly affect the results, and a dedicated analysis is required to estimate and subtract its contribution.

Given the morphology of G21.5−0.9, and its small relative size comparable to the IXPE angular resolution, it is expected that the effect of polarization leakage will be particularly relevant in the outskirts of the PWN. Its contribution was evaluated using different techniques, including a full IXPESIM/IXPEOBSSIM (N. Di Lalla 2019) simulation of the source using GEANT4 (S. Agostinelli et al. 2003), the Mueller matrix formalism described in N. Bucciantini et al. (2023a), a hybrid machine learning and analytic track reconstruction method (N. Cibrario et al. 2023), and, finally, the recently released LeakageLib package (J. T. Dinsmore & R. W. Romani 2024). The latter tool, in particular, implements the most accurate model of the polarization leakage to date using in-flight calibrated 2D point-spread functions (PSFs), and its routines allow the user to predict the leakage pattern based on a CXO image and subtract it from the measured IXPE polarization map. A detailed summary of the different approaches can be found in Appendix B. Despite methodological differences, all four techniques yield consistent polarization structures within uncertainties, confirming the robustness of the analysis, particularly in the central, high-significance region of the PWN.

Figure 3 shows the detected IXPE polarization pattern, overlaid on top of the deep CXO count map of G21.5−0.9 zoomed over the PWN region. The effect of polarization leakage has been estimated and subtracted with LeakageLib, using the same CXO image to model the source. The measured polarization is visualized using a set of segments, one per pixel, whose length and inclination represent the local PD (in scale) and PA (measured east of north). The segment color indicates the level of significance of the detection: green corresponds to measurements with significance >3σ, black to those between 2σ and 3σ. For comparison, white segments represent the polarization pattern measured in the radio band (P. C. W. Lai et al. 2022). Measurements with polarization consistent with

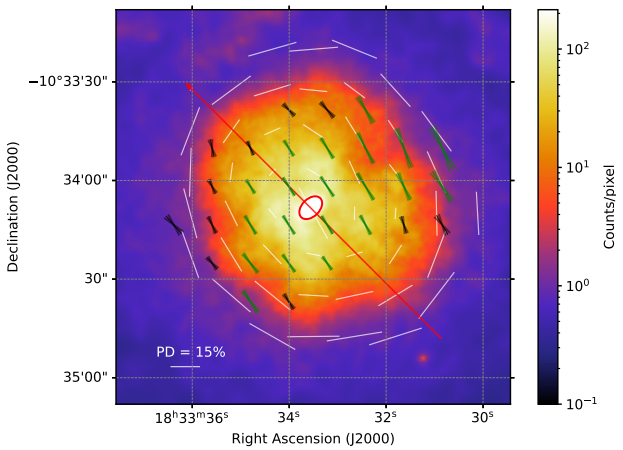

Figure 3. Leakage-subtracted polarization map of the PWN as determined from the space-resolved analysis (2–8 keV) in a 0.′1944 grid. Each pixel is correlated with its neighbors as described in the text. The length and orientation of the arrows represent the measured local PD and PA. The black and green lines are the IXPE polarization measurements with a $>2\sigma$ and $>3\sigma$ significance, respectively, with additional two sets of lines of the same colors (but different orientation) indicating the associated 1σ uncertainty on the PA. The white, tangentially distributed lines are the polarization structure observed in radio (P. C. W. Lai et al. 2022), corresponding to a radial magnetic field configuration. At the bottom-left corner is the reference arrow length for PD = 15%. The red arrow represents the projected spin-axis direction of PSR J1833−1034 of ∼45° (C. Y. Ng & R. W. Romani 2008). The red ellipse roughly corresponds to the region of the inner compact nebula where a high level of polarization was measured in the infrared (A. Zajczyk et al. 2012). The background image is the deep CXO image zoomed in over the PWN.

zero within 2σ are not shown. As shown in Figure 3, the detected pattern in the central region of the PWN, where the statistical significance is highest, is roughly consistent with a constant PD of 11%–12% at an angle of 30°–35°. In the outer regions, the detection is generally less significant due to lower photon statistics. While the measured PD and PA values in these regions appear to vary slightly across the nebula, they are most likely still consistent with a uniform polarization pattern when accounting for their larger uncertainties and the systematics introduced by the leakage correction. This apparent variation, along with the inclusion of regions where no significant polarization was observed—such as the southwest portion of the PWN (bottom right)—helps explain why the space-integrated analysis (Section 3.1), which includes the entire PWN, yielded a lower average PD. The only notable exception is the northwest region (top right), where the PD increases progressively, reaching values as high as 20–30% with a PA around 20°–25°. No significant polarization was detected outside the PWN.

4. Discussion

Polarization studies provide a powerful diagnostic tool for probing the magnetic field structure and particle acceleration mechanisms in PWNe. In the case of G21.5−0.9, IXPE observations allow us to explore the polarization properties of the X-ray-emitting electrons and compare them with those observed in the radio band. This comparison offers crucial insights into the evolution of the PWN's magnetic field and its interaction with the surrounding SNR environment.

The model that assumes the same outer polarization structure observed in the radio band—where the magnetic field is predominantly radial with respect to the pulsar—predicts that, in an annulus with inner and outer radii of 30″ and 60″, respectively, the PA should be tangential, with a background-subtracted and leakage-corrected PD ≃20% ± 5%. Using the `xpstokesalign` tool of IXPEOBSSIM, we aligned the reconstructed Stokes parameters of this region to a tangential (radio-like) polarization model by rotating the Stokes vectors event by event, based on their spatial position. Despite an MDP of ∼10%, we did not find evidence of significant polarization. This result strongly suggests that the magnetic field structures traced by the radio- and X-ray-emitting electrons are different. In this respect, G21.5−0.9 appears more similar to the Crab Nebula than to Vela, where the radio and X-ray polarization structures are well aligned (F. Xie et al. 2022; K. Liu et al. 2023). Interestingly, both G21.5−0.9 and the Crab Nebula are believed to be in the free-expansion phase, where the PWN expands into the cold SNR ejecta (N. Bucciantini et al. 2003) and strong Rayleigh–Taylor instabilities shape the outer regions (B.-I. Jun 1998; N. Bucciantini et al. 2004). Vela, on the other hand, is likely in a later evolutionary phase, where interaction with the SNR reverse shock is modifying the structure and dynamics of the nebula (E. van der Swaluw et al. 2003).

Given that G21.5−0.9 is at the resolution limit of IXPE, we cannot directly determine which specific nebular structures contribute most to the observed polarization. In particular, two competing scenarios remain indistinguishable: (i) a highly polarized central torus dominating the polarized emission of the source, as suggested by infrared observations (A. Zajczyk et al. 2012), or (ii) a bulk PWN magnetic field that is more uniform but with a lower degree of polarization (∼10%). However, the latter scenario is inconsistent with radio observations, which show a clearly radial magnetic field pattern (P. C. W. Lai et al. 2022).

To evaluate the possible contribution of a highly polarized torus, we simulated two different scenarios using IXPEOBSSIM: (i) a uniformly polarized torus embedded in an unpolarized nebula, and (ii) the same torus within a nebula that follows the polarization structure and degree observed in the radio band at 5 GHz (P. C. W. Lai et al. 2022). In both cases, the polarized torus is modeled as an elliptical region ($3\farcs3 \times 7\farcs0$) with uniform polarization, centered on the CXO X-ray intensity peak and oriented with a position angle on the plane of the sky of 30°, consistent with the measured PA and predictions from magnetohydrodynamic models. We varied the torus PD and PA in the simulations until we achieved consistency with the polarization properties measured in the central region of the PWN (space-integrated `PCUBE` analysis within a radius 20″ from the PSR: PD =12% ± 2%, PA =34° ± 5°). This region was chosen because it provides the highest polarization significance while minimizing leakage effects, which are not simulated by IXPEOBSSIM (see Appendix B.2). The results of these simulations for the two model configurations are shown in Table 3. Both models yield large uncertainties in the intrinsic polarization properties of the torus, and neither scenario is strongly favored, though the unpolarized nebula case appears somewhat closer to the infrared observations. In either case, the results are consistent with previous IXPE studies of other PWNe (F. Xie et al. 2022; N. Bucciantini et al. 2023b; R. W. Romani et al. 2023), suggesting that even in the case of G21.5−0.9, close to the termination shock—where particles are likely being accelerated to high energies—turbulence remains moderate ($\delta B/B$ at most ∼0.8–1), indicating a relatively ordered magnetic field.

Table 3
Torus and Nebula Models

Nebula Model	Torus PD	Torus PA
Unpolarized	44% ± 7%	34° ± 5°
Radio-like polarized	37% ± 7%	29° ± 5°

Note. Different model configurations for the inner torus and nebula that reproduce the polarization properties measured by IXPE in the central region of the PWN. The intrinsic polarization values for the torus are obtained through model fitting using IXPEOBSSIM simulations for each nebula configuration.

The PA measured by IXPE for G21.5−0.9 in the space-integrated analysis differs by approximately 3σ from the spin-axis orientation of PSR J1833−1034 inferred from morphological modeling of the X-ray torus (C. Y. Ng & R. W. Romani 2008). This discrepancy may be explained by the fact that the IXPE measurement reflects the integrated polarization from the entire PWN, including contributions from the more extended outer regions, rather than isolating the compact torus. As demonstrated by our simulations (Table 3), even small residual polarization from the outer nebula or deviations from perfect axisymmetry can bias the inferred PA away from the spin-axis direction. A similar effect has been observed in the Crab Nebula (N. Bucciantini et al. 2023b), where nonaxisymmetric surface brightness in the X-ray torus produces a measurable offset between PA and the PWN symmetry axis. Given these considerations and the modest statistical tension, we regard the measured PA and spin-axis orientation as broadly consistent within uncertainties.

Our findings suggest that a two-zone model for G21.5−0.9 is probably preferred: a central bright X-ray torus dominated by a globally toroidal magnetic field, surrounded by an outer layer affected by Rayleigh–Taylor instabilities, similar to the filamentary network seen in the Crab Nebula, which stretches the magnetic field radially. However, the overall low integrated polarization of G21.5−0.9 distinguishes this source from other well-studied PWNe like the Crab, Vela, and MSH 15−52. This fact, along with differences in the radio polarization pattern and the absence of a strong jet-torus structure, suggests that X-ray-emitting particles may populate a larger region of the PWN where turbulence is stronger or where magnetic field geometry varies significantly due to internal dynamics or enhanced diffusion.

Acknowledgments

The Imaging X-ray Polarimetry Explorer (IXPE) is a joint US and Italian mission. The US contribution is supported by the National Aeronautics and Space Administration (NASA) and led and managed by its Marshall Space Flight Center (MSFC), with industry partner Ball Aerospace (contract NNM15AA18C). The Italian contribution is supported by the Italian Space Agency (Agenzia Spaziale Italiana, ASI) through contract ASI-OHBI-2022-13-I.0, agreements ASI-INAF-2022-19-HH.0 and ASI-INFN-2017.13-H0, and its Space Science Data Center (SSDC) with agreements ASI-INAF-2022-14-HH.0 and ASI-INFN 2021-43-HH.0, and by the Istituto Nazionale di Astrofisica (INAF) and the Istituto Nazionale di Fisica Nucleare (INFN) in Italy. This research used data products provided by the IXPE Team (MSFC, SSDC, INAF, and INFN) and distributed with additional software tools by the High-Energy Astrophysics Science Archive Research Center (HEASARC), at NASA Goddard Space Flight Center (GSFC). R.F., E.Co., A.D.M., S.F., F.L.M., F.Mu., and P.So. are partially supported by MAECI with grant CN24GR08 "GRBAXP: Guangxi Rome Bilateral Agreement for X-ray Polarimetry in Astrophysics." C.-Y.N. is supported by a GRF grant of the Hong Kong Government under HKU 17304524. N.B. was supported by the INAF MiniGrant "PWNnumpol—Numerical Studies of Pulsar Wind Nebulae in The Light of IXPE." F.X. is supported by National Natural Science Foundation of China (grant Nos. 12373041 and 12422306), and Bagui Scholars Program (XF). I.L. was funded by the European Union ERC-2022-STG – BOOTES – 101076343. Views and opinions expressed are however those of the author (s) only and do not necessarily reflect those of the European Union or the European Research Council Executive Agency. Neither the European Union nor the granting authority can be held responsible for them.

Facilities: IXPE, CXO.

Software: IXPEOBSSIM (L. Baldini et al. 2022), IXPESIM (N. Di Lalla 2019), `3ML` (G. Vianello et al. 2015), `LeakageLib` (J. T. Dinsmore & R. W. Romani 2024).

Appendix A
Spectropolarimetric Analysis

In this section of the appendix, we provide additional plots to support the spectropolarimetric analysis of the entire PWN, as described in Section 3.1. Figure 4 presents the Stokes I, Q, and U spectra for the three DUs, along with their best-fit models and the residuals from the `3ML` analysis. While the Stokes Q and U spectra are well described by the model, the Stokes I spectral fit shows significant deviations at low energies, most likely due to instrumental calibration issues. These discrepancies become more noticeable as the statistical uncertainties approach the level of systematic errors. To assess the potential impact of these issues on the polarization measurement, we repeated the same analysis in two additional configurations: (i) applying the off-axis vignetting correction to the on-axis IXPE effective area (version `20240125`, used throughout the paper) using the HEASARC tool `ixpecalcarf`,[58] and (ii) employing the previous time-independent version of the IXPE IRFs (version `20230526`, released on 2023 June 16). In both cases, while the best-fit power-law index Γ varied within the range 1.85–1.98, the resulting PD and PA values remained virtually unchanged.

The IXPE energy response matrix is defined in 275 channels spanning 1–12 keV (0.04 keV per bin), and we analyzed the resulting spectra without additional rebinning, as in other IXPE studies (M. Negro et al. 2023). We verified that rebinning the data to coarser energy grids (e.g., 25 or 100 bins over 2–8 keV) does not affect the spectropolarimetric results. Given the featureless, nonthermal nature of the source spectrum, we find no need to apply optimized rebinning schemes such as that proposed by J. S. Kaastra & J. A. M. Bleeker (2016). Overall, despite the minor calibration uncertainties that affect the spectral analysis, the stability of the polarization measurements confirms the robustness and reliability of our polarimetric results.

[58] https://heasarc.gsfc.nasa.gov/docs/software/lheasoft/help/ixpecalcarf.py.html

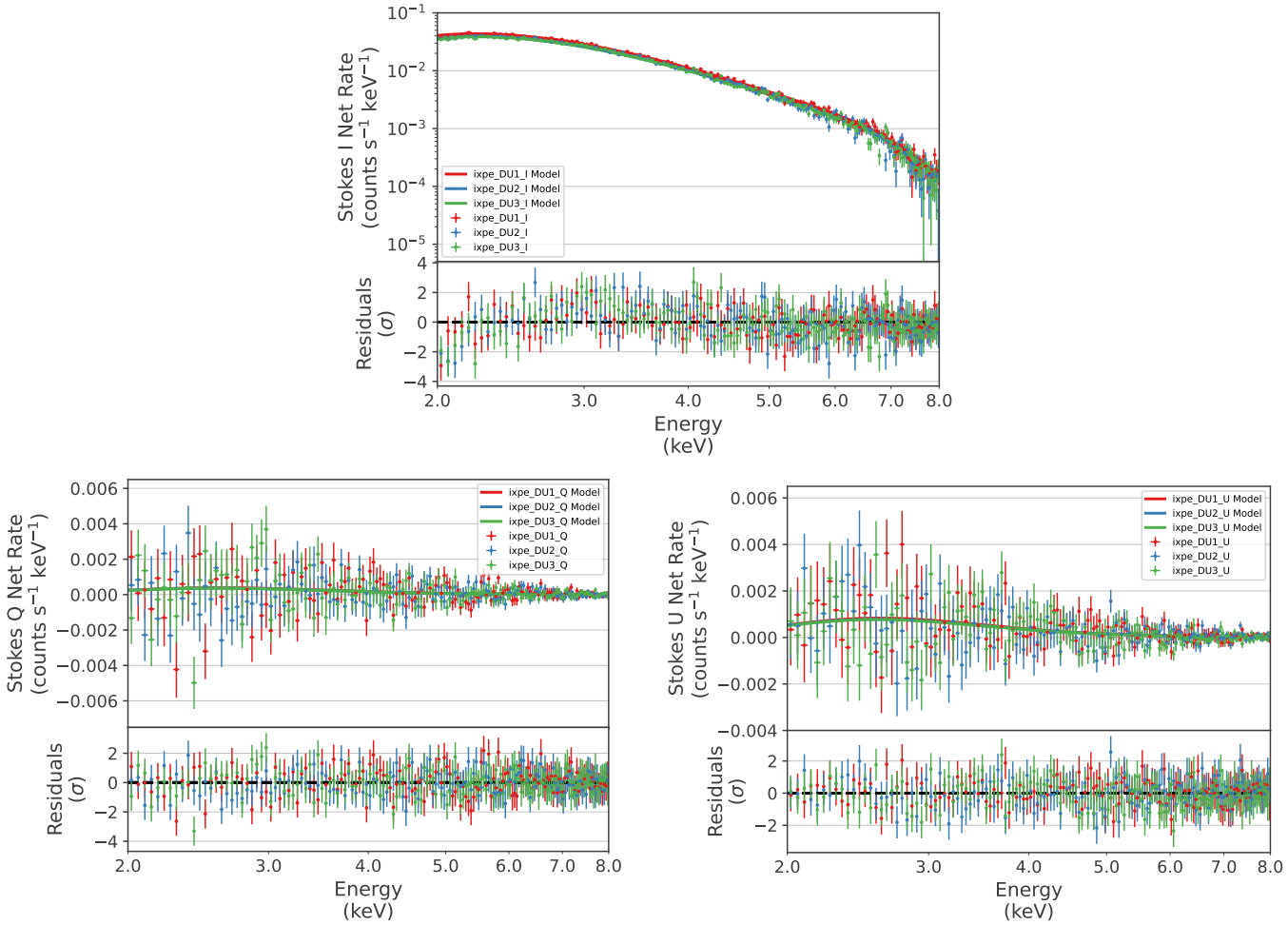

Figure 4. Stokes parameter I (top), Q (bottom left), and U spectra (bottom right) for the three DUs (shown in red, blue, and green), along with best-fit models and the residuals from the the `3ML` analysis (IRFs version `20240125`).

Appendix B
Polarization Leakage Evaluation and Correction

Figure 5 shows the uncorrected polarization map of G21.5 −0.9 obtained from the space-resolved analysis (2–8 keV). Compared to Figure 3, the outer regions appear to exhibit an outflow pattern, which results from the superposition of the intrinsic, nearly uniform polarization of the source and the radial footprint introduced by polarization leakage. In this appendix, we provide a detailed comparison of the different techniques used to evaluate and correct the effect of polarization leakage, which is particularly relevant for spatially resolved polarimetric analyses of extended sources such as G21.5−0.9. The purpose of this comparison is to validate the robustness of the recovered polarization morphology shown in Figure 3.

As reported in Section 3.2, four independent techniques were employed: the `LeakageLib` software package, a full IXPESIM/IXPEOBSSIM simulation of the source, a joint machine learning and analytic event reconstruction method, and the Mueller matrix approach, each one described in the sections below. Although each method has some limitations, `LeakageLib` is currently the most advanced correction technique and was used to generate Figure 3. Figure 6 provides

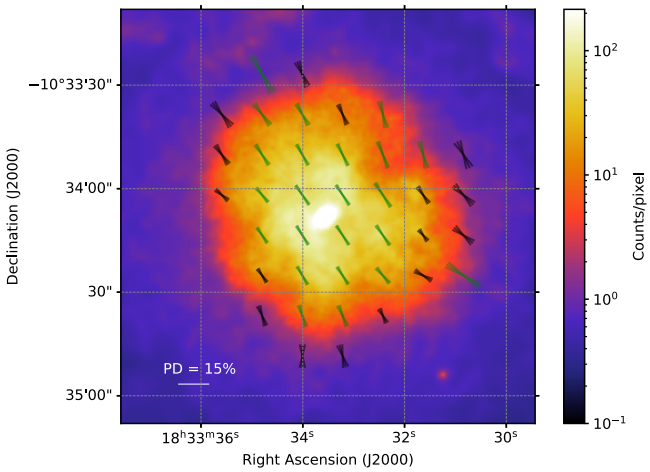

Figure 5. Polarization map of the PWN as determined from the space-resolved analysis (2–8 keV) in a 0.1944′ grid not corrected for the effect of the polarization leakage. As in Figure 3, each pixel is correlated with its neighbors, and the length and orientation of the arrows represent the measured local PD and PA. At the bottom-left corner is the reference arrow length for PD = 15%. The black and green lines have a $>2\sigma$ and $>3\sigma$ significance, respectively. The background image is a CXO image zoomed in over the PWN.

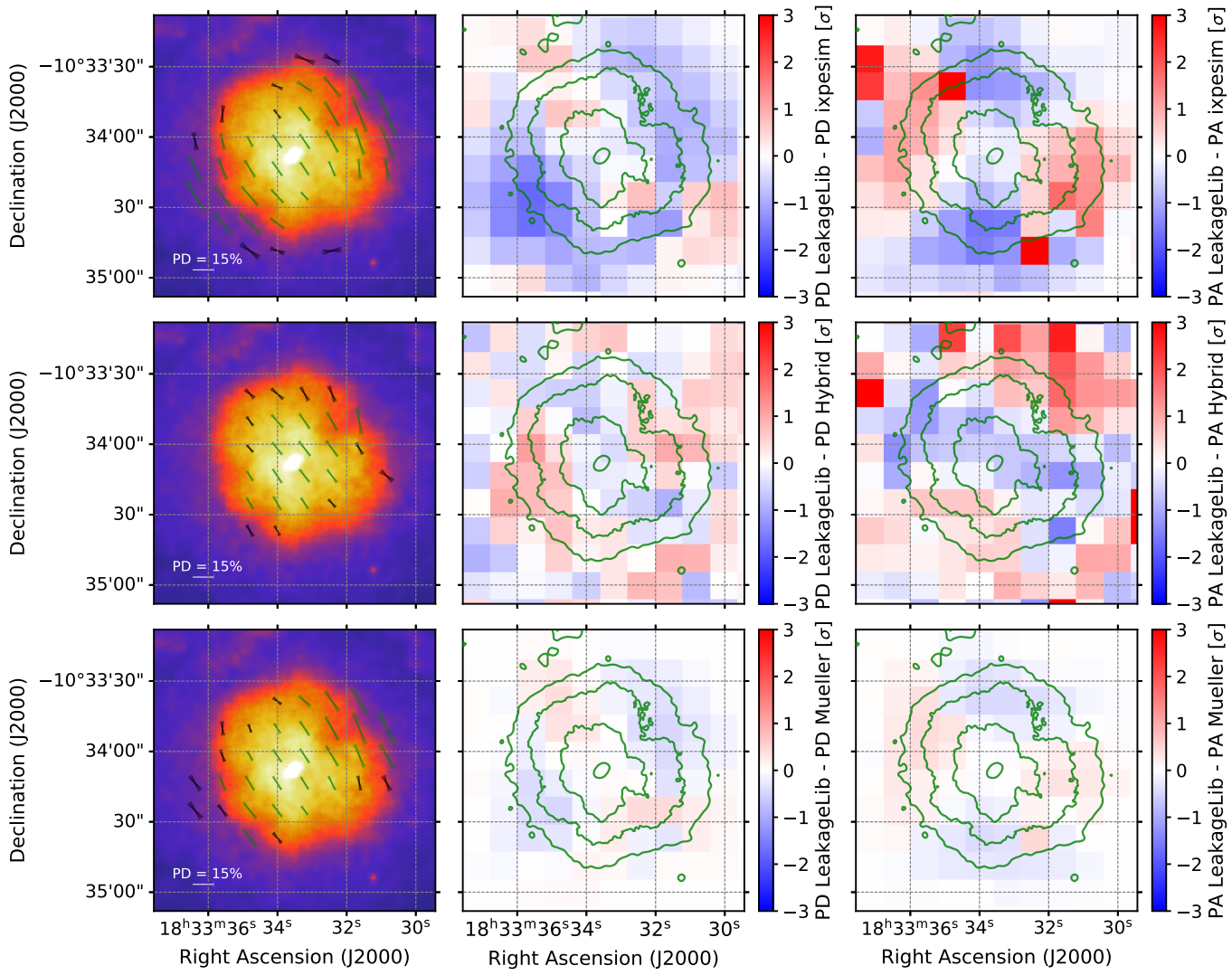

Figure 6. Detailed comparison between the result of the different methods used to estimate and subtract or mitigate the effect of polarization leakage. Going from the top to the bottom, the three rows show the outcome of the IXPESIM/IXPEOBSSIM simulation, the hybrid event reconstruction method, and the Mueller matrix approach. The first column shows the corrected polarization maps obtained with each method (2–8 keV). The background image is a Chandra observation zoomed in over the PWN, and the polarization measurement is shown using the same convention as Figure 5. The second and third columns display the differences in the PD and PA leakage-corrected maps for each method, relative to the `LeakageLib` result, rescaled by the sum in quadrature of the corresponding uncertainties. Despite methodological differences, all techniques yield broadly consistent results for both PD and PA across the PWN, confirming the robustness of the polarization analysis.

a side-by-side comparison of the polarization maps obtained using the three alternative methods relative to `LeakageLib`, chosen as a reference. The leftmost column of each row shows the corrected polarization map using the indicated method, while the middle and right columns show the residuals in PD and PA compared to `LeakageLib`, expressed in units of combined uncertainty. The `LeakageLib` and Mueller matrix methods yield nearly identical outcomes, while the hybrid event reconstruction provides an independent confirmation by directly mitigating leakage effects. The IXPESIM/IXPEOBSSIM simulation slightly overestimates leakage correction but remains within acceptable limits. While small variations exist at the edges of the nebula, where leakage and systematic uncertainties become more prominent, the general structure is stable across methods. Overall, all four techniques yield broadly consistent polarization patterns—especially in the bright, central region of the PWN where the statistical significance is highest—reinforcing confidence in our polarization leakage correction techniques and the robustness of our polarization analysis.

B.1. LeakageLib

The `LeakageLib` (J. T. Dinsmore & R. W. Romani 2024) package introduces a new model and algorithm for correcting polarization leakage in IXPE data. Compared to the linearized approach of the Mueller matrix formalism, described later in Appendix B.4, this method allows for a more general correlation between the spatial offset of the reconstructed impact point and the inferred polarization direction. Thanks to the implementation of a 2D displacement model which accounts for both longitudinal and transverse components of the offset, the formalism implemented in `LeakageLib` can be applied to a more general model of the PSF, not necessarily azimuthally symmetric. To better represent the data, this software uses a set of sky-calibrated 2D PSFs, one for each

IXPE telescope, derived from a set of bright, weakly polarized point sources observed by IXPE.

For extended sources, the tool provides routines to estimate the expected Stokes maps (I, Q, and U) due to polarization leakage based on a CXO observation of the source. The CXO count map is assumed to represent the true morphology given its far superior angular resolution compared to IXPE. However, in the current release (v1.1.0), no dependence on the IXPE PSF off-axis angle or event energy has yet been implemented. For G21.5−0.9, we modeled the source using the same CXO map employed throughout the paper. The output Stokes maps, containing the predicted signal induced by leakage, are then normalized to match the observed data and properly rebinned using the same grid as in Figure 5. For all IXPE telescopes, the content of the Stokes Q and U maps is finally subtracted from the polarization map obtained in Section 3.2.

B.2. IXPESIM/IXPEOBSSIM Simulation

The IXPEOBSSIM (L. Baldini et al. 2022) software allows the user to simulate an IXPE observation starting from a generic model of the source or a CXO observation. However, IXPEOBSSIM alone cannot predict polarization leakage, as this effect is not included in the standard IRFs. To enable leakage prediction, IXPEOBSSIM offers an interface to IXPESIM (N. Di Lalla 2019), which implements a detailed photon-by-photon `GEANT4` simulation of the physical interactions in the GPD. As described in the official documentation,[59] a list of photons can be simulated in IXPEOBSSIM up to the beryllium window on top of the GPD using the `xpphotonlist` application. These photons are then propagated throughout the detector using IXPESIM and turned into a list of actual photoelectron tracks for the events that trigger the detector. The output file containing the track images (comparable to the IXPE Level-1 data) can be reconstructed using the same event reconstruction algorithm used for the flight data, and a final step using `xpsimfmt`, part of IXPEOBSSIM, closes the loop by formatting it in a way virtually identical to the actual IXPE Level-2 data.

Based on a CXO observation of G21.5−0.9 (ObsID 5166), we ran 100 full IXPESIM/IXPEOBSSIM simulations, equivalent to a total exposure time of 40 Ms. We modeled the source as intrinsically unpolarized, so that any pattern detected in the output polarization map could be attributed to the leakage effect. By rescaling and rebinning the resulting Stokes maps with the same binning scheme as in Figure 5, their contribution can be subtracted pixelwise to correct the polarization leakage effect. The top row of Figure 6 shows a detailed comparison between the outcome of the IXPESIM/IXPEOBSSIM simulation technique and `LeakageLib`. In contrast to all other methods, this approach appears to overcorrect the leakage effect, inducing a spurious tangential pattern. Previous validation studies involving simpler cases, such as point sources, have shown that the IXPESIM/IXPEOBSSIM approach tends to systematically overestimate the level of polarization leakage, likely due to an imperfect tuning of the detector parameters in IXPESIM, given the observed time evolution of the GPD. Nevertheless, the differences measured between the two methods are within 3σ, although clearly spatially correlated due to the overprediction of the leakage amplitude by the simulation.

[59] https://ixpeobssim.readthedocs.io/en/latest/ixpesim.html

B.3. Hybrid Event Reconstruction

Hybrid event reconstruction is a recently developed method, described in detail in N. Cibrario et al. (2023), which combines a new machine-learning-based prediction of the photon impact point with a standard moment analysis reconstruction of the photoelectron track, commonly used for IXPE data. This joint approach exploits the better performance achieved by convolutional neural networks in predicting the conversion points from the track images, improving the IXPE polarization capabilities (expressed by the modulation factor) and partially mitigating the effect of polarization leakage (N. Cibrario et al. 2025).

We reprocessed the IXPE Level-1 data of this observation, publicly available on the HEASARC archive along with the Level-2 data, using the hybrid event reconstruction method. This technique is particularly valuable for comparison, as it is the only approach that directly mitigates polarization leakage rather than subtracting it. Thus, it provides an independent and complementary assessment. As described in Section 3.2, we binned the reprocessed data following the same recipe using the `PMAP` algorithm of `xpbin` to produce a new polarization map. The central row of Figure 6 shows the map resulting from this method and its comparison with `LeakageLib`. Despite the different methodology, the results in the high-significance region of the PWN are fully consistent with `LeakageLib` within 1σ.

B.4. Mueller Matrix Formalism

The Mueller matrix approach, thoroughly discussed in N. Bucciantini et al. (2023a), is essentially a generalization of the PSF for polarized observations, where the elements of the Mueller matrix describe how the intrinsic Stokes parameters mix with each other due to the effect of polarization leakage. The primary assumption of this method is that the displacement of the reconstructed absorption point from the true position is correlated with the direction of the reconstructed polarization plane (preferentially displaced along the direction of the polarization plane). This simplifies the problem to a linear displacement model. The matrix elements can be derived either theoretically from a given PSF or by fitting the expected functional form using in-flight IXPE data. In either case, computing the Stokes maps of any source is reduced to a simple convolution with a CXO count map. For G21.5−0.9, we adopted parameters derived from the IXPE observation of Cygnus X-1 (ObsID 01002901), one of the brightest, weakly polarized point sources observed by IXPE. Unlike `LeakageLib`, the tool implementing this formalism assumes a circular, azimuthally symmetric PSF, such as that provided by IXPEOBSSIM. Although this is an approximation of the real PSF (see J. T. Dinsmore & R. W. Romani 2024 for a detailed comparison), this model still provides a reasonable estimate of the average effect across the three IXPE telescopes. As previously done for `LeakageLib`, the leakage estimation is based on a CXO observation of G21.5−0.9, and the resulting Stokes maps are properly normalized, rebinned, and finally subtracted from the uncorrected polarization map, to allow a meaningful comparison. As for the other methods, the subtracted polarization map and its comparison with `LeakageLib` is reported in Figure 6 (bottom row). The results of these two methods are in excellent agreement, with differences in the PD and PA maps well below 1σ, most likely due to differences in PSF parameterization.

ORCID iDs

Niccolò Di Lalla https://orcid.org/0000-0002-7574-1298
Nicola Omodei https://orcid.org/0000-0002-5448-7577
Niccolò Bucciantini https://orcid.org/0000-0002-8848-1392
Jack T. Dinsmore https://orcid.org/0000-0002-6401-778X
Nicolò Cibrario https://orcid.org/0000-0003-3842-4493
Stefano Silvestri https://orcid.org/0000-0002-8665-0105
Josephine Wong https://orcid.org/0000-0001-6395-2066
Patrick Slane https://orcid.org/0000-0002-6986-6756
Tsunefumi Mizuno https://orcid.org/0000-0001-7263-0296
Michela Negro https://orcid.org/0000-0002-6548-5622
Roger W. Romani https://orcid.org/0000-0001-6711-3286
Riccardo Ferrazzoli https://orcid.org/0000-0003-1074-8605
C.-Y. Ng https://orcid.org/0000-0002-5847-2612
Miltiadis Michailidis https://orcid.org/0009-0008-3653-1109
Yi-Jung Yang https://orcid.org/0000-0001-9108-573X
Fei Xie https://orcid.org/0000-0002-0105-5826
Martin C. Weisskopf https://orcid.org/0000-0002-5270-4240
Philip Kaaret https://orcid.org/0000-0002-3638-0637
Iván Agudo https://orcid.org/0000-0002-3777-6182
Lucio A. Antonelli https://orcid.org/0000-0002-5037-9034
Matteo Bachetti https://orcid.org/0000-0002-4576-9337
Luca Baldini https://orcid.org/0000-0002-9785-7726
Wayne H. Baumgartner https://orcid.org/0000-0002-5106-0463
Ronaldo Bellazzini https://orcid.org/0000-0002-2469-7063
Stefano Bianchi https://orcid.org/0000-0002-4622-4240
Stephen D. Bongiorno https://orcid.org/0000-0002-0901-2097
Raffaella Bonino https://orcid.org/0000-0002-4264-1215
Alessandro Brez https://orcid.org/0000-0002-9460-1821
Fiamma Capitanio https://orcid.org/0000-0002-6384-3027
Simone Castellano https://orcid.org/0000-0003-1111-4292
Elisabetta Cavazzuti https://orcid.org/0000-0001-7150-9638
Chien-Ting Chen https://orcid.org/0000-0002-4945-5079
Stefano Ciprini https://orcid.org/0000-0002-0712-2479
Enrico Costa https://orcid.org/0000-0003-4925-8523
Alessandra De Rosa https://orcid.org/0000-0001-5668-6863
Ettore Del Monte https://orcid.org/0000-0002-3013-6334
Laura Di Gesu https://orcid.org/0000-0002-5614-5028
Alessandro Di Marco https://orcid.org/0000-0003-0331-3259
Immacolata Donnarumma https://orcid.org/0000-0002-4700-4549
Victor Doroshenko https://orcid.org/0000-0001-8162-1105
Michal Dovčiak https://orcid.org/0000-0003-0079-1239
Steven R. Ehlert https://orcid.org/0000-0003-4420-2838
Teruaki Enoto https://orcid.org/0000-0003-1244-3100
Yuri Evangelista https://orcid.org/0000-0001-6096-6710
Sergio Fabiani https://orcid.org/0000-0003-1533-0283
Javier A. Garcia https://orcid.org/0000-0003-3828-2448
Shuichi Gunji https://orcid.org/0000-0002-5881-2445
Jeremy Heyl https://orcid.org/0000-0001-9739-367X
Wataru Iwakiri https://orcid.org/0000-0002-0207-9010
Svetlana G. Jorstad https://orcid.org/0000-0001-6158-1708
Vladimir Karas https://orcid.org/0000-0002-5760-0459
Fabian Kislat https://orcid.org/0000-0001-7477-0380
Jeffery J. Kolodziejczak https://orcid.org/0000-0002-0110-6136
Henric Krawczynski https://orcid.org/0000-0002-1084-6507
Fabio La Monaca https://orcid.org/0000-0001-8916-4156
Luca Latronico https://orcid.org/0000-0002-0984-1856
Ioannis Liodakis https://orcid.org/0000-0001-9200-4006
Simone Maldera https://orcid.org/0000-0002-0698-4421
Alberto Manfreda https://orcid.org/0000-0002-0998-4953
Frédéric Marin https://orcid.org/0000-0003-4952-0835
Andrea Marinucci https://orcid.org/0000-0002-2055-4946
Alan P. Marscher https://orcid.org/0000-0001-7396-3332
Herman L. Marshall https://orcid.org/0000-0002-6492-1293
Francesco Massaro https://orcid.org/0000-0002-1704-9850
Giorgio Matt https://orcid.org/0000-0002-2152-0916
Fabio Muleri https://orcid.org/0000-0003-3331-3794
Stephen L. O'Dell https://orcid.org/0000-0002-1868-8056
Chiara Oppedisano https://orcid.org/0000-0001-6194-4601
Alessandro Papitto https://orcid.org/0000-0001-6289-7413
George G. Pavlov https://orcid.org/0000-0002-7481-5259
Abel Lawrence Peirson https://orcid.org/0000-0001-6292-1911
Matteo Perri https://orcid.org/0000-0003-3613-4409
Melissa Pesce-Rollins https://orcid.org/0000-0003-1790-8018
Pierre-Olivier Petrucci https://orcid.org/0000-0001-6061-3480
Maura Pilia https://orcid.org/0000-0001-7397-8091
Andrea Possenti https://orcid.org/0000-0001-5902-3731
Juri Poutanen https://orcid.org/0000-0002-0983-0049
Simonetta Puccetti https://orcid.org/0000-0002-2734-7835
Brian D. Ramsey https://orcid.org/0000-0003-1548-1524
John Rankin https://orcid.org/0000-0002-9774-0560
Ajay Ratheesh https://orcid.org/0000-0003-0411-4243
Oliver J. Roberts https://orcid.org/0000-0002-7150-9061
Carmelo Sgró https://orcid.org/0000-0001-5676-6214
Paolo Soffitta https://orcid.org/0000-0002-7781-4104
Gloria Spandre https://orcid.org/0000-0003-0802-3453
Douglas A. Swartz https://orcid.org/0000-0002-2954-4461
Toru Tamagawa https://orcid.org/0000-0002-8801-6263
Fabrizio Tavecchio https://orcid.org/0000-0003-0256-0995
Roberto Taverna https://orcid.org/0000-0002-1768-618X
Allyn F. Tennant https://orcid.org/0000-0002-9443-6774
Nicholas E. Thomas https://orcid.org/0000-0003-0411-4606
Francesco Tombesi https://orcid.org/0000-0002-6562-8654
Alessio Trois https://orcid.org/0000-0002-3180-6002
Sergey Tsygankov https://orcid.org/0000-0002-9679-0793
Roberto Turolla https://orcid.org/0000-0003-3977-8760
Jacco Vink https://orcid.org/0000-0002-4708-4219
Kinwah Wu https://orcid.org/0000-0002-7568-8765
Silvia Zane https://orcid.org/0000-0001-5326-880X

References

Abdo, A. A., Ajello, M., Allafort, A., et al. 2013, ApJS, 208, 17
Agostinelli, S., Allison, J., Amako, K., et al. 2003, NIMPA, 506, 250
Baldini, L., Barbanera, M., Bellazzini, R., et al. 2021, APh, 133, 102628
Baldini, L., Bucciantini, N., Di Lalla, N., et al. 2022, SoftX, 19, 101194
Becker, R. H., & Kundu, M. R. 1976, ApJ, 204, 427
Becker, R. H., & Szymkowiak, A. E. 1981, ApJL, 248, L23

Bellazzini, R., Angelini, F., Baldini, L., et al. 2006, NIMPA, 560, 425
Bietenholz, M. F., & Bartel, N. 2008, MNRAS, 386, 1411
Bietenholz, M. F., Matheson, H., Safi-Harb, S., Brogan, C., & Bartel, N. 2011, MNRAS, 412, 1221
Bocchino, F., van der Swaluw, E., Chevalier, R., & Bandiera, R. 2005, A&A, 442, 539
Bucciantini, N., Amato, E., Bandiera, R., Blondin, J. M., & Del Zanna, L. 2004, A&A, 423, 253
Bucciantini, N., Blondin, J. M., Del Zanna, L., & Amato, E. 2003, A&A, 405, 617
Bucciantini, N., Di Lalla, N., Romani, R. W. R., et al. 2023a, A&A, 672, A66
Bucciantini, N., Ferrazzoli, R., Bachetti, M., et al. 2023b, NatAs, 7, 602
Camilo, F., Ransom, S. M., Gaensler, B. M., et al. 2006, ApJ, 637, 456
Cibrario, N., Negro, M., Bonino, R., et al. 2025, ApJ, 984, 171
Cibrario, N., Negro, M., Moriakov, N., et al. 2023, A&A, 674, A107
Di Lalla, N. 2019, PhD thesis, Univ. Pisa https://etd.adm.unipi.it/t/etd-04042019-100412
Di Marco, A., Soffitta, P., Costa, E., et al. 2023, AJ, 165, 143
Dinsmore, J. T., & Romani, R. W. 2024, ApJ, 962, 183
Furst, E., Handa, T., Morita, K., et al. 1988, PASJ, 40, 347
Gaensler, B. M., & Slane, P. O. 2006, ARA&A, 44, 17
Guest, B. T., Safi-Harb, S., & Tang, X. 2019, MNRAS, 482, 1031
Gupta, Y., Mitra, D., Green, D. A., & Acharyya, A. 2005, CSci, 89, 853
Hewish, A., Bell, S. J., Pilkington, J. D. H., Scott, P. F., & Collins, R. A. 1968, Natur, 217, 709
Jun, B.-I. 1998, ApJ, 499, 282
Kaastra, J. S., & Bleeker, J. A. M. 2016, A&A, 587, A151
Kislat, F., Clark, B., Beilicke, M., & Krawczynski, H. 2015, APh, 68, 45
Lai, P. C. W., Ng, C. Y., & Bucciantini, N. 2022, ApJ, 930, 1
Liu, K., Xie, F., Liu, Y.-H., et al. 2023, ApJL, 959, L2
Matheson, H., & Safi-Harb, S. 2005, AdSpR, 35, 1099
Matheson, H., & Safi-Harb, S. 2010, ApJ, 724, 572
Negro, M., Di Lalla, N., Omodei, N., et al. 2023, ApJL, 946, L21
Ng, C. Y., & Romani, R. W. 2008, ApJ, 673, 411
Romani, R. W., Wong, J., Di Lalla, N., et al. 2023, ApJ, 957, 23
Safi-Harb, S., Harrus, I. M., Petre, R., et al. 2001, ApJ, 561, 308
Slane, P., Chen, Y., Schulz, N. S., et al. 2000, ApJL, 533, L29
Smith, D. A., Abdollahi, S., Ajello, M., et al. 2023, ApJ, 958, 191
Tian, W. W., & Leahy, D. A. 2008, MNRAS, 391, L54
Tsujimoto, M., Guainazzi, M., Plucinsky, P. P., et al. 2011, A&A, 525, A25
van der Swaluw, E., Achterberg, A., Gallant, Y. A., Downes, T. P., & Keppens, R. 2003, A&A, 397, 913
Vianello, G., Lauer, R. J., Younk, P., et al. 2016, ICRC (The Hague), 34, 1042
Weisskopf, M. C., Elsner, R. F., & O'Dell, S. L. 2010, Proc. SPIE,
Weisskopf, M. C., Soffitta, P., Baldini, L., et al. 2022, JATIS, 8, 026002
Wilms, J., Allen, A., & McCray, R. 2000, ApJ, 542, 914
Wilson, A. S., & Weiler, K. W. 1976, A&A, 53, 89
Xie, F., Di Marco, A., La Monaca, F., et al. 2022, Natur, 612, 658
Zajczyk, A., Gallant, Y. A., Slane, P., et al. 2012, A&A, 542, A12